INFLUENCE OF D-TYPE ROUGHNESS ON A SELF-SIMILAR ADVERSE PRESSURE GRADIENT TURBULENT BOUNDARY LAYER

Ziqi Chen, Bihai Sun, Alireza Heidarian, Callum Atkinson and Julio Soria
Laboratory for Turbulence Research in Aerospace and Combustion (LTRAC)
Department of Mechanical and Aerospace Engineering
Monash University
Clayton, 3800, Victoria, Australia
ziqi.chen@monash.edu

ABSTRACT

The development of an adverse pressure gradient (APG)-turbulent boundary layer (TBL) over d-type roughness was experimentally investigated in the LTRAC APG-TBL wind tunnel. A dual-camera two-component, two-dimensional (2C-2D) particle image velocimetry (PIV) system was implemented to simultaneously capture the outer-layer structure and near-wall behaviour. The roughness consists of uniformly spaced square elements, with a roughness-to-boundary-layer ratio of $k/\delta = 0.03$. Measurements are conducted at three streamwise stations, spanning a domain of $2.97\,\delta^*$, where δ^* is the reference boundary-layer thickness measured at x^* which is 0.03 m downstream from the roughness leading edge. The first- and second-order statistics obtained at the top centres of crest and valley locations are compared with a smooth-wall self-similar adverse pressure gradient turbulent boundary layer (SS-APG-TBL) reference to quantify the influence of d-type roughness. The mean velocity profiles collapse above both crest and valley locations for $y/\delta > 10^{-2}$, with significant differences in the near-wall region attributed to the local roughness geometry. All Reynolds stresses are elevated above smooth-wall values for $3 \times 10^{-3} < y/\delta < 0.5$, while collapsing with the smooth-wall reference for $y/\delta > 0.5$, indicating that the APG dominates the outer region.

INTRODUCTION

Surface roughness is ubiquitous in engineering applications and plays a critical role in shaping the structure of TBLs. By modifying near-wall turbulence structures, surface roughness alters the mechanisms governing skin friction, momentum transport, and aerodynamic performance. Consequently, the study of flows over rough walls is of significant practical importance for the accurate prediction of drag and lift.

Rough-wall turbulent boundary layers under zero pressure gradient (ZPG) have been extensively studied and serve as canonical reference flows. Classical studies show that the primary effect of surface roughness is a downward shift of the logarithmic mean velocity profile, commonly quantified by the roughness function, ΔU^+, relative to the smooth-wall case (Clauser, 1956; Perry & Joubert, 1963). In the fully rough regime, this shift becomes essentially independent of viscosity and depends primarily on the roughness geometry (Jiménez, 2004). A related cornerstone in rough-wall turbulence is Townsend's outer-layer similarity hypothesis (Townsend, 1976), which proposes that, when the roughness height is small compared with the boundary-layer thickness, roughness effects are primarily confined to the near-wall region, while the outer layer remains approximately similar to that over a smooth wall when scaled with appropriate outer variables. Nevertheless, deviations from outer-layer similarity have been reported when the roughness scale is sufficiently large, or when roughness-induced wall-normal transport modifies the outer-layer turbulence structure (Bhaganagar *et al.*, 2004).

The validity of Townsend's hypothesis is further complicated in the presence of pressure gradients, which alter both the structure and scaling of TBLs. Boundary layers subjected to APG exhibit markedly different behaviour from their ZPG counterparts, including enhanced boundary-layer growth, amplified outer-layer turbulence, and an increased propensity for flow separation (Skåre & Krogstad, 1994). Systematic investigation of such flows remains challenging because of history effects, whereby flow statistics depend not only on local conditions but also on the cumulative influence of upstream pressure-gradient development.

Mellor & Gibson (1966) defined an equilibrium APG-TBL as a state in which the imposed streamwise pressure-gradient acting over the displacement thickness of the boundary layer is balanced by the wall shear stress. This condition is characterised by a constant Clauser pressure-gradient parameter (Clauser, 1954), $\beta = \frac{\delta_1}{\tau_w}\frac{dP}{dx}$, where δ_1 is the displacement thickness, τ_w is the wall shear stress, and $\frac{dP}{dx}$ is the far-field pressure gradient. Under these conditions, the boundary layer develops under an approximately constant pressure-gradient history. Based on this concept, Skåre & Krogstad (1994) experimentally established an equilibrium turbulent boundary layer close to separation, characterised by low and nearly constant skin friction. Later, Shehzad *et al.* (2023) adapted this approach and applied it to the LTRAC APG-TBL wind tunnel, allowing the boundary layer to achieve self-similar development. In this state, the mean flow and turbulence statistics, when appropriately scaled with local velocity and length scales, remain approximately invariant in the streamwise direction, as demonstrated by Chen *et al.* (2026*a*,*b*).

The present study experimentally investigates the response of an established smooth-wall SS-APG-TBL to a change in wall condition from hydraulically smooth to d-type rough. The rough-wall case is generated in the same LTRAC APG-TBL wind-tunnel configuration and under the same imposed pressure-gradient distribution as the smooth-wall reference case of Chen *et al.* (2026*b*). A dual-camera 2C-2D PIV approach is used to resolve both the near-wall region and the outer layer, enabling the modification of the boundary layer by the imposed roughness to be assessed relative to the original smooth-wall self-similar state.

EXPERIMENTAL FACILITY

The experiments were carried out in the Laboratory for Turbulence Research in Aerospace and Combustion (LTRAC) APG-TBL wind tunnel. The flow is driven by a 5.5 kW centrifugal fan, passes through flow straighteners, then a 10:1 contraction before entering the 4.5 m long and 1.0 m wide test section equipped with a variable-geometry roof, as shown in Figure 1. The test section design has a spanwise-to-boundary-layer aspect ratio of 6.7, which eliminates sidewall influences. Optical access was enabled by glass side walls. The adverse pressure gradient is imposed using a contoured roof adjusted by eight lifting rods, allowing a turbulent boundary layer close to incipient separation. To maintain the flow at the verge of separation, the rate of roof-height variation is gradually reduced downstream. The roof profile was originally proposed by Skåre & Krogstad (1994) and subsequently adapted by Shehzad *et al.* (2023) for the LTRAC facility. This design results in a strong APG upstream, followed by a relaxation of the pressure gradient within the region of interest (ROI). On the smooth wall, a self-similar APG-TBL is established at the verge of separation with approximately constant $\beta = 18.8$ in the ROI on a smooth wall (Chen *et al.*, 2026*b*).

Within the ROI, the smooth wall is replaced by a 500-mm-long d-type roughness plate, with its leading edge locates 2.5 m downstream of the tripping device. For the present study, the streamwise coordinate system is defined with $x = 0$ at the leading edge of the roughness plate, as illustrated in Figure 2a. The roughness elements is uniformly spaced, with width and height $w = k = 5$ mm. The reference length scale δ^* is defined as the boundary-layer thickness at $x^* = 0.03$, yielding a roughness-to-boundary-layer ratio of $k/\delta^* = 0.03$ as shown in Figure 2b.

DUAL-CAMERA 2C-2D PIV SETUP

A dual-camera PIV system is used to simultaneously capture the large-scale motions in the outer region of the turbulent boundary layer and resolve the near-wall flow. This arrangement is required because the measurement imposes competing demands on field of view and spatial resolution: resolving the near-wall gradients requires high magnification, whereas capturing the outer-layer motions requires a sufficiently large field of view (FOV). A single-camera configuration cannot satisfy both requirements without compromising either near-wall resolution or outer-layer spatial coverage.

The system consists of two Imperx B6640 CCD cameras arranged in a vertical stack, each with a 6600×4400 pixel sensor and a pixel pitch of 5.5 μm. The cameras are synchronised to acquire 12-bit double-exposure image pairs at 1 Hz. The large field of view (LFV) camera, fitted with a 100 mm Zeiss lens, provides a FOV of approximately $1.3\delta(H) \times 0.9\delta(W)$ in the streamwise–wall-normal plane, with an optical scale of 30.5 μm/px. The high-spatial-resolution (HSR) camera, equipped with a 200 mm Nikon Micro-Nikkor lens, is focused on the near-wall region and provides a smaller FOV of $0.3\delta(H) \times 0.5\delta(W)$, with an optical scale of 12.2 μm/px. The optical parameters and PIV interrogation-window settings for both cameras are summarised in Table 1. The lower edge of both FOVs extends approximately 1 mm below the roughness crest plane, allowing the roughness geometry to be resolved in the images. Measurements are performed at three streamwise locations separated by 1δ, as illustrated in Figure 2a.

Illumination is provided by a dual-cavity Nd:YAG laser (NewWave Solo 200XT), which delivers 3–5 ns pulses with a maximum pulse energy of 200 mJ at 10 Hz. The light-sheet thickness at the ROI, measured using burn paper, is approximately 1 mm. Image acquisition is synchronised with the laser pulses to record double-exposure particle images.

A water–glycerol mixture is used to generate seeding droplets with an approximate diameter of 1 μm. The droplets are introduced upstream through the centrifugal fan and distributed throughout the ROI.

Table 1: Camera optical parameters, and PIV interrogation window(IW) settings for the LFV and HSR systems, where a 50 % overlap between adjacent windows.

Parameter	**LFV**	**HSR**
Lens	Zeiss 100 mm F2 Zf.2 Makro	Nikon 200 mm $f/4$ AF Micro-Nikkor
$f/\#$	2	4
SR [μm/px]	30.5	12.2
First pass window		
[px]	96×32	128×64
[mm]	2.93×0.98	1.56×0.78
[$\Delta x/k \times \Delta y/k$]	0.57×0.19	0.30×0.15
[$\Delta x/\delta^* \times \Delta y/\delta^*$]	0.02×0.01	0.01×0.01
Final pass window		
[px]	32×8	64×8
[mm]	0.98×0.24	0.78×0.10
[$\Delta x/k \times \Delta y/k$]	0.19×0.05	0.15×0.02
[$\Delta x/\delta^* \times \Delta y/\delta^*$] $\times 10^{-2}$	0.66×0.16	0.59×0.07

LENS DISTORTION CORRECTION AND CAMERA POSITION CALIBRATION

A calibration target with a 5 mm grid spacing is used to determine the camera positions and correct for lens distortion. The distortion mapping functions are modelled using a third-order polynomial mapping that includes both radial and tangential components (Soloff *et al.*, 1997). The polynomial coefficients are obtained by least-squares fitting (Levenberg, 1944), yielding residual errors below one pixel for each camera. The mapping functions are then applied directly to the spatial coordinates of the PIV velocity vectors, following Sun *et al.* (2021). This coordinate-based correction avoids remapping the particle images or interpolating the velocity fields, thereby improving computational efficiency.

The camera overlap region is determined from the distortion-corrected calibration images. The distortion-corrected LFV image is interpolated onto the same optical scale as the HSR image, after which cross-correlation is performed over the full overlap region to estimate the relative displacement between the two camera fields. The resulting residual registration errors are within $4 pixels = 48.8 \mu m$ on the HSR-resolution grid in both the x- and y-directions. Since the optical scale of the LFV camera is approximately 2.4 times coarser than that of the HSR camera, this level of mismatch is consistent with the residual uncertainty associated with the distortion correction.

2C-2D PIV PROCESSING

At each station, a total of 12,000 velocity fields are obtained using a multigrid/multipass cross-correlation PIV algorithm (Soria, 1996). The corresponding processing parameters are listed in Table 1. Sub-pixel accuracy was achieved by fitting a two-dimensional Gaussian function to the correlation peak, yielding an uncertainty of approximately 0.06 pixels at the 95 % confidence level (Soria, 1996).

Vector validation is performed using both correlation-level and vector-level criteria. Correlation-level validation employed a neighbourhood-based correction involving eight surrounding interrogation windows (Hart, 2000). Vector-level validation applies a maximum-displacement criterion of 0.2 of the interrogation-window size, with a 50 % overlap between adjacent windows. Final-pass window sizes were optimised for each camera and measurement station. Vector validation involved a maximum-displacement criterion (0.2 window size) together with the normalised median test with a threshold of 2.0 (Westerweel & Scarano, 2005). Invalid vectors were replaced using χ^2-based polynomial interpolation from 13 neighbouring vectors, thereby reducing spurious gradients (Soria, 1996; Fouras & Soria, 1998).

For each station, a reference grid was defined in the streamwise direction such that LFV grid points coincided with a subset of this grid, while the finer HSR measurements were interpolated onto the same reference positions. This procedure preserved the higher spatial resolution of the HSR data while ensuring consistency and continuity across the overlap between the two cameras.

In the wall-normal direction, a three-region composite-grid strategy is used. In the near-wall region, $y < 0.15\delta$, the lower portion of the HSR field of view is used to providing fine spatial resolution close to the roughness. In the transition region, $0.15\delta < y < 0.3\delta$, a geometric growth ratio of 1.004 is used to smoothly bridge the two grid resolutions, and the HSR and LFV datasets are combined using a weighted averaged. In the outer region, $y > 0.3\delta$, the grid spacing of the LFV velocity field is used to maintain full boundary-layer coverage. This composite-grid retains the near-wall resolution of the high-resolution system while preserving the outer-layer coverage of the large-field-of-view measurements. The weighting function follows that described by (Chen *et al.*, 2026*b*).

RESULTS AND DISCUSSION

Table 2 presents the characteristic velocity and length scales at the three measurement stations. The boundary-layer thickness, δ, is defined as the wall-normal location corresponding to the onset of the irrotational core in the far field of the APG-TBL. The characteristic velocity, U_∞, is defined as the mean streamwise velocity at the boundary-layer edge, taken here at $y = \delta$, and is used as the reference velocity for outer scaling.

In the present study, the wall-normal origin is defined at the roughness crest height, which coincides with the smooth-wall level, as shown in Figure 2a. As shown in Figure 3, δ increases approximately linearly across the ROI, while U_∞ decreases in the streamwise direction as expected.

Table 2: Characteristic velocity and length scales at three measurement stations, measured at the crest-height level above the centre of each crest and valley location. The crest and valley indices of the roughness elements are measured from the start of the roughness plate, as illustrated in Figure 2b.

On the Crest			
Location $\tilde{x}/\delta^*$	Crest Index	U_∞ [m/s]	δ [mm]
0.66	10	7.62	150.1
1.68	25	7.47	158.0
2.71	40	7.32	166.3
On the Valley			
Location $\tilde{x}/\delta^*$	Valley Index	U_∞ [m/s]	δ [mm]
0.63	10	7.62	151.3
1.65	25	7.47	159.0
2.68	40	7.32	165.5

The first- and second-order statistics of the APG-TBL subject to the imposed d-type roughness are presented in Figure 4, normalised by the local boundary-layer thickness, δ, and the characteristic velocity, U_∞. The profiles are compared with the smooth-wall SS-APG-TBL reference of Chen *et al.* (2026*b*).

The mean velocity profiles in Figure 4a collapse across all crest and valley measurement locations for $y/\delta > 10^{-2}$. In the near-wall region, $y/\delta < 10^{-2}$, clear differences are observed between the crest and valley profiles, indicating that the local roughness geometry modifies the near-wall mean flow. Differences from the smooth-wall reference are also observed for $y/\delta > 6 \times 10^{-2}$, suggesting that the response to the imposed roughness is not confined strictly to the immediate near-wall region, but extends into part of the outer layer. This behaviour is consistent with previous observations of rough-wall APG-TBLs reported by Tsikata & Tachie (2013). Above the roughness crests, the profiles initially follow the smooth-wall trend for $y/\delta < 2 \times 10^{-3}$, consistent with the no-slip condition at the crest surface, before increasing more rapidly than the smooth-wall reference at larger wall-normal distances.

The Reynolds stresses, $\overline{uu}$, $\overline{vv}$, and $-\overline{uv}$, are examined to assess how the change in wall condition modifies turbulence intensities and momentum transport under the imposed APG, as shown in Figure 4b, Figure 4c, and Figure 4d. The stresses are normalised by U_∞^2 and collapse across all crest and valley measurement locations for $y/\delta > 2 \times 10^{-2}$, indicating that the outer-scaled profiles are approximately invariant over the measured streamwise range away from the immediate near-wall region. Compared with the smooth-wall reference, the rough-wall stresses are elevated over $3 \times 10^{-3} < y/\delta < 0.5$ and exhibit a single outer peak near $y/\delta \approx 0.5$. For $y/\delta > 0.5$, the rough-wall Reynolds stresses approach the smooth-wall reference, suggesting that the outermost region is less sensitive to the imposed roughness than the near-wall and intermediate regions.

The component-wise behaviour reveals that the influence of roughness is not identical for all stress components. The $\overline{uu}/U_\infty^2$ profile shows the strongest elevation relative to the smooth-wall reference, extending from the near-wall region to the outer peak at $y/\delta \approx 0.5$, indicating enhanced streamwise velocity fluctuations beyond the immediate vicinity of the roughness elements. Near the wall, the profiles measured at different streamwise locations do not collapse, and this streamwise variation is most pronounced in $\overline{uu}/U_\infty^2$. In the very near-wall region, $y/\delta < 3 \times 10^{-3}$, the valley measurements exhibit larger streamwise fluctuations than both the smooth-wall and crest cases, consistent with recirculating motions within the cavities between roughness elements (Jiménez, 2004). Similar near-wall deviations are observed in the $\overline{vv}/U_\infty^2$ and $-\overline{uv}/U_\infty^2$ profiles, however, these deviations persist up to $y/\delta < 2 \times 10^{-2}$, suggesting that the wall-normal and Reynolds-shear-stress components are more sensitive to roughness-induced modification of the near-wall flow.

CONCLUSIONS

The present study experimentally investigates the response of a smooth-wall SS-APG-TBL to a change in wall condition from hydraulically smooth to uniformly spaced square d-type roughness elements, with $\lambda/k = 2$ and $k/\delta = 0.03$. The rough-wall case is generated under the same imposed pressure-gradient configuration as the smooth-wall reference. A dual-camera PIV approach is employed to resolve both the roughness-affected near-wall region and the outer-layer development.

The mean velocity profiles collapse above both crest and valley locations for $y/\delta > 10^{-2}$, indicating that the roughness-induced modification of the mean flow is primarily confined to the near-wall region under the present scaling. Below this height, clear crest–valley differences are observed, demonstrating the influence of the local roughness geometry. Differences from the smooth-wall reference are also observed farther from the wall, suggesting that the response to the imposed roughness is not limited strictly to the immediate roughness sublayer.

The Reynolds stresses, $\overline{uu}/U_\infty^2$, $\overline{vv}/U_\infty^2$, and $-\overline{uv}/U_\infty^2$, are elevated relative to the smooth-wall reference over $3 \times 10^{-3} < y/\delta < 0.5$, with an outer peak near $y/\delta \approx 0.5$. For $y/\delta > 0.5$, the rough-wall profiles approach the smooth-wall reference, suggesting reduced sensitivity to roughness in the outermost region. Near the wall, the profiles measured at different streamwise locations do not collapse, with this variation most pronounced in $\overline{uu}/U_\infty^2$. The elevated valley profiles of $\overline{uu}/U_\infty^2$ are consistent with recirculating motions within the roughness cavities, while $\overline{vv}/U_\infty^2$ and $-\overline{uv}/U_\infty^2$ show near-wall elevations that persist to $y/\delta < 2 \times 10^{-2}$.

ACKNOWLEDGEMENT

This material is based upon work supported by the Air Force Office of Scientific Research (AFOSR) under award number FA2386-24-1-4025. The authors also acknowledge the computational resources provided by the Pawsey Supercomputing Centre, supported by the Australian and Western Australian Governments, and the National Computational Infrastructure (NCI), supported by the Australian Government through computational grants awarded by the National Computational Merit Allocation Scheme (NCMAS) funded by the Australian Government. Z. Chen is supported by an AFOSR funded Monash University Graduate Scholarship.

REFERENCES

Bhaganagar, Kiran, Kim, John & Coleman, Gary 2004 Effect of roughness on wall-bounded turbulence. *Flow, turbulence and combustion* **72** (2), 463–492.

Chen, Ziqi, Sun, Bihai, Heidarian, Alireza, Atkinson, Callum & Soria, Julio 2026*a* Experimental study of a high-reynolds-number self-similar adverse pressure gradient turbulent boundary layer at the verge of separation. In *Journal of Physics: Conference Series*, , vol. 3173, p. 012014. IOP Publishing.

Chen, Ziqi, Sun, Bihai, Heidarian, Alireza, Atkinson, Callum & Soria, Julio 2026*b* High-spatial-resolution piv measurements of a self-similar adverse pressure gradient turbulent boundary layer at the verge of separation. *Experimental Thermal and Fluid Science* p. 111730.

Clauser, F. H. 1954 Turbulent boundary layers in adverse pressure gradients. *Journal of the Aeronautical Sciences* **21** (2), 91–108.

Clauser, Francis H 1956 The turbulent boundary layer. *Advances in applied mechanics* **4**, 1–51.

Fouras, A. & Soria, J. 1998 Accuracy of out-of-plane vorticity measurements derived from in-plane velocity field data. *Experiments in Fluids* **25**, 409–430.

Hart, D. P. 2000 PIV error correction. *Experiments in Fluids* **29** (1), 13–22.

Jiménez, J. 2004 Turbulent flows over rough walls. *Annual Review of Fluid Mechanics* **36**, 173–196.

Levenberg, Kenneth 1944 A method for the solution of certain non-linear problems in least squares. *Quarterly of applied mathematics* **2** (2), 164–168.

Mellor, GL & Gibson, DM 1966 Equilibrium turbulent boundary layers. *Journal of Fluid Mechanics* **24** (2), 225–253.

Perry, A. E. & Joubert, P. N. 1963 Rough-wall boundary layers in adverse pressure gradients. *Journal of Fluid Mechanics* **17** (2), 193–211.

Shehzad, Muhammad, Sun, Bihai, Atkinson, Callum & Soria, Julio 2023 Characterisation of a self-similar turbulent boundary layer near separation measured using high-spatial-resolution two-component - two-dimensional particle image velocimetry. *arXiv Preprint* .

Skåre, Per Egil & Krogstad, Per-Åge 1994 A turbulent equilibrium boundary layer near separation. *Journal of Fluid Mechanics* **272**, 319–348.

Soloff, Steven M, Adrian, Ronald J & Liu, Zi-Chao 1997 Distortion compensation for generalized stereoscopic particle image velocimetry. *Measurement science and technology* **8** (12), 1441–1454.

Soria, J. 1996 An investigation of the near wake of a circular cylinder using a video-based digital cross-correlation particle image velocimetry technique. *Experimental Thermal and Fluid Science* **12**, 221–233.

Sun, B., Shehzad, M., Jovic, D., Cuvier, C., Willert, C., Ostovan, Y., Foucaut, J. M., Atkinson, C. & Soria, J. 2021 Distortion correction of two-component two-dimensional PIV using a large imaging sensor with application to measurements of a turbulent boundary layer flow at $Re_\tau = 2386$. *Experiments in Fluids* **62** (9), 183.

Townsend, A. A. 1976 *The structure of turbulent shear flow*, 2^{nd} edn. Cambridge University Press.

Tsikata, JM & Tachie, MF 2013 Effects of roughness and adverse pressure gradient on the turbulence structure. *International journal of heat and fluid flow* **44**, 239–257.

Westerweel, J. & Scarano, F. 2005 Universal outlier detection for PIV data. *Experiments in Fluids* **39** (6), 1096–1100.

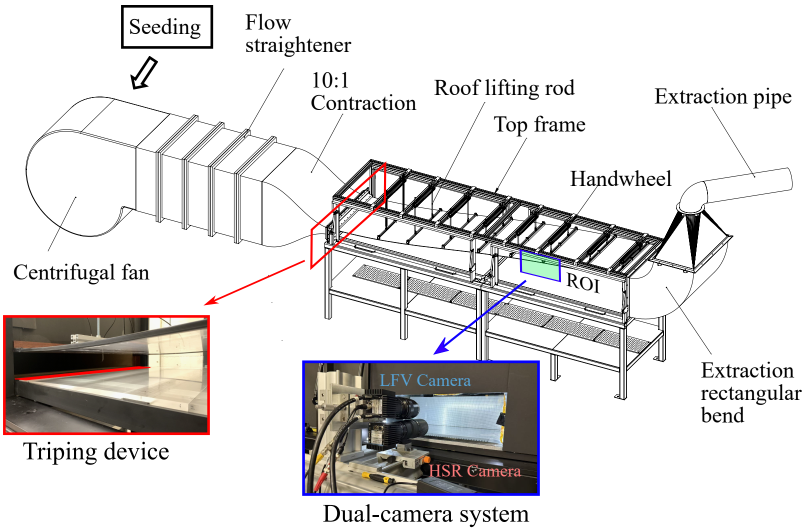

Figure 1: 3D model of the LTRAC APG-TBL wind tunnel (Chen *et al.*, 2026*a*,*b*). The region of interest (□) starts at 2.53 m downstream of the tripping device (□) along the centreline of the tunnel, and the flow is measured by a dual-camera system (□).

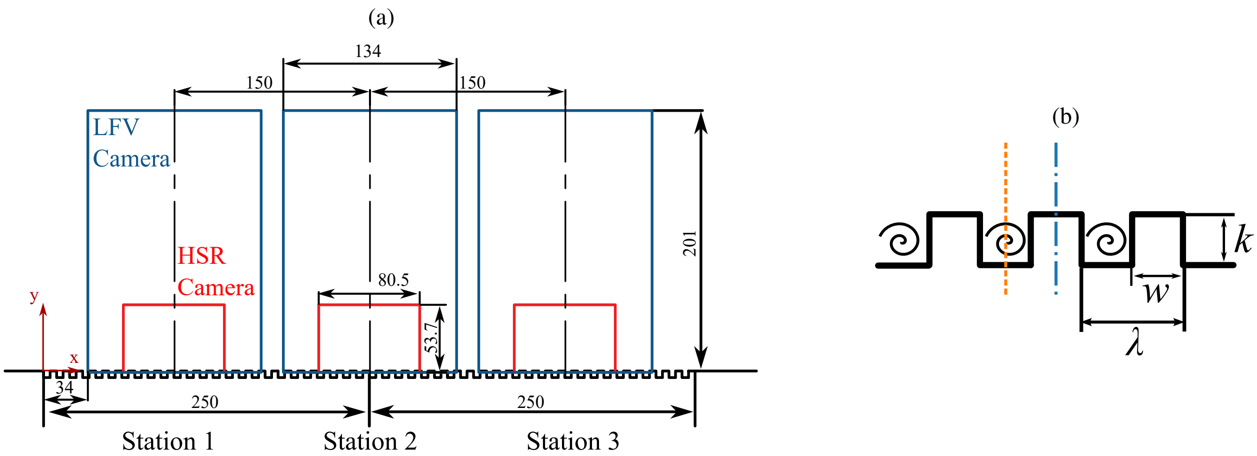

Figure 2: (a) FOVs for the three measurement stations, shown in mm, where the origin of the streamwise coordinate is defined at the leading edge of the roughness plate. (b) Schematic of the d-type roughness element illustrating the vortex within the groove, where $k = w = 5$ mm and $\lambda = 10$ mm, measurements were taken on the centre of the valleys (- - -) and the centre of the following crests (– · –).

Figure 3: (a) The boundary-layer thickness δ fitted with a linear function (- - -), and (b) free-stream velocity U_∞ along the streamwise direction in the ROI. Measurements were taken at the centres of the valleys between roughness elements at $x/\delta^* = 0.63$ (▲), 1.65 (■), and 2.68 (♦), and at the centres of the crests of the roughness elements at $x/\delta^* = 0.66$ (▲), 1.68 (■), and 2.71 (♦).

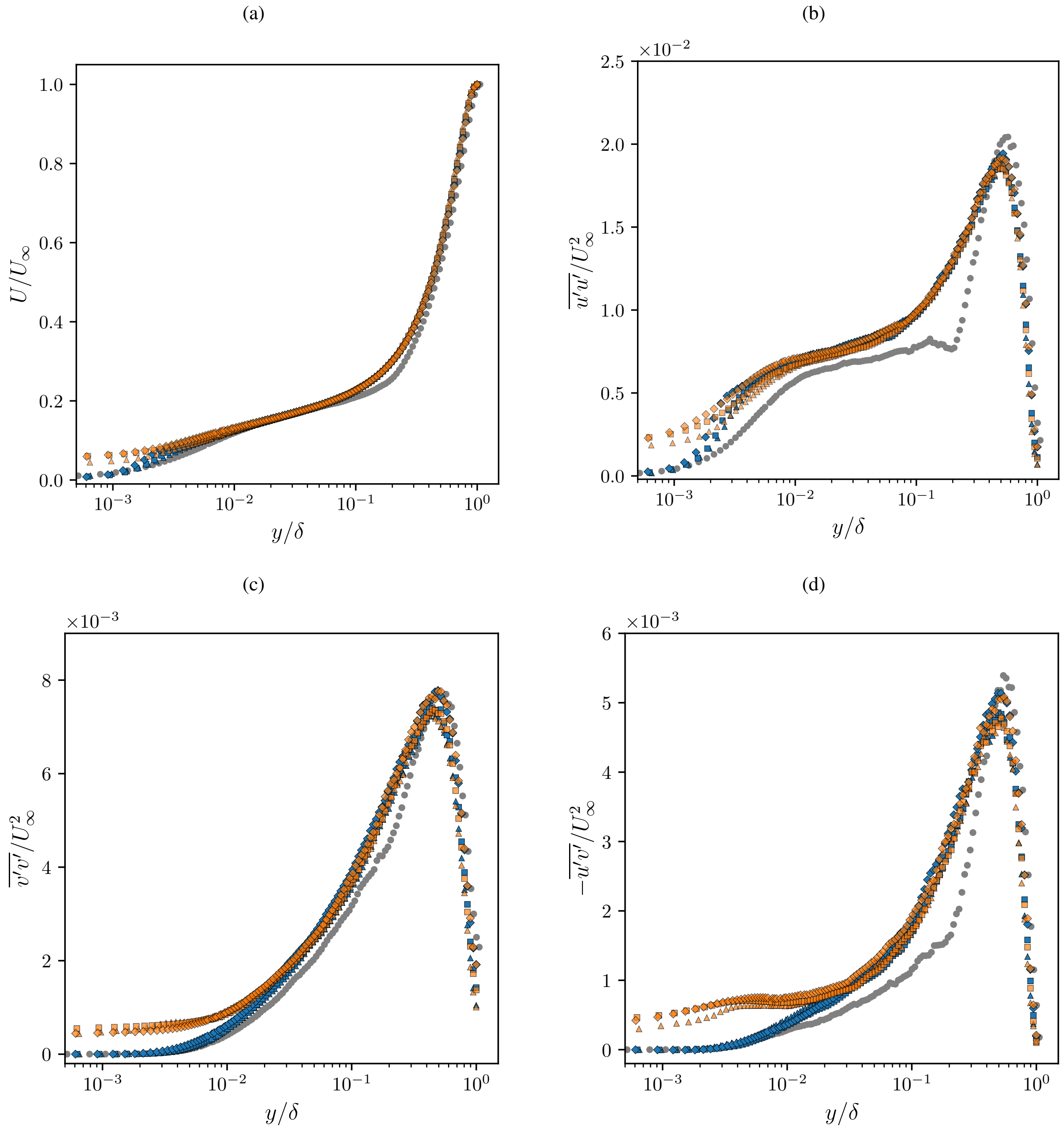

Figure 4: The ensemble-averaged profiles of the APG-TBL over the rough wall, scaled with U_∞ and δ: (a) the mean velocity, and the Reynolds stresses: (b) $\overline{u'u'}$, (c) $\overline{v'v'}$, and (d) $-\overline{u'v'}$. The profiles are compared with a self-similar APG-TBL over a smooth wall (●) under the same imposed pressure distribution reported by Chen *et al.* (2026*b*). For plotting clarity, the profiles were subsampled to 150 points along the wall-normal direction using logarithmic spacing.